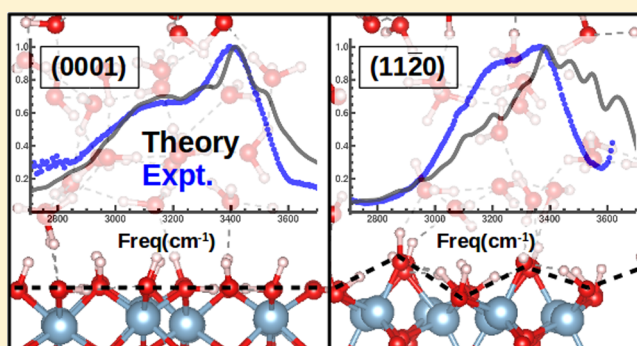


Relating Interfacial Order to Sum Frequency Generation with Ab Initio Simulations of the Aqueous $\text{Al}_2\text{O}_3(0001)$ and $(11\bar{2}0)$ InterfacesMark DelloStritto,^{†,‡,§} Stefan M. Piontek,[†] Michael L. Klein,^{†,‡,§} and Eric Borguet^{*,†,‡}[†]Department of Chemistry, [‡]Center for the Computational Design of Functional Layered Materials, and [§]Institute for Computational Molecular Science, Temple University, Philadelphia, Pennsylvania 19122, United States

Supporting Information

ABSTRACT: We use density functional theory molecular dynamics simulations to investigate the structure, dynamics, and vibrational sum frequency generation (vSFG) spectra at the $\text{Al}_2\text{O}_3(0001)\text{-H}_2\text{O}$ and $\text{Al}_2\text{O}_3(11\bar{2}0)\text{-H}_2\text{O}$ interfaces. We find that the differences in the vSFG spectra between the two interfaces can be explained by significantly weaker surface–water interactions at the (0001) vs (11 $\bar{2}0$) interface. The weaker interactions at the (0001) surface are caused by the flat surface plane and high density of OH groups, leading to a decoupling of the vibrational modes of the surface OH groups and H_2O molecules. The (0001) vSFG spectrum thus displays two well-separated peaks at the near-neutral pH, in contrast to the vSFG spectrum of the corrugated (11 $\bar{2}0$) interface, which has stronger surface–water interactions and thereby a narrower band in the vSFG spectrum with closely spaced peaks. By simulating the interfaces with both the Perdew–Burke–Ernzerhof (PBE)–Tkatchenko–Scheffler and revised PBE (RPBE) functionals, we find that a proper description of the separation of surface and solution H-bond modes is essential to obtain accurate SFG spectra. The RPBE functional was unable to accurately model the H-bonds of H_2O and surface aluminols simultaneously. Finally, we use the H-bond lifetimes and the tetrahedral order parameter for H_2O to conclude that water at the (0001) surface is more ordered than at the (11 $\bar{2}0$) surface, in contrast to prior interpretations of X-ray reflectivity and vSFG experiments, highlighting the importance of atomistic models of the H-bond structure and dynamics of the water–oxide interfaces.



INTRODUCTION

Liquid water is one of the most interesting physical systems to study; unlike simple liquids with weak or nearly isotropic interactions, water is a structured liquid with strong anisotropic interactions.^{1,2} The structure of water is due to the presence of strong H-bonds between H_2O molecules, which, when combined with the tetrahedral charge distribution of the H_2O molecule, result in the presence of an extended, tetrahedral H-bond network. This structured nature of water is particularly important at aqueous interfaces, as solid surfaces can modify water structure, display different charges across a range of pH values, and can preferentially adsorb different ions at different surface sites. The interface between water and oxide minerals is particularly interesting, as water either dissociates on contact with the exposed metals atoms or is strongly bound to the surface,^{3–5} resulting in a surface effectively covered with OH groups. The two-dimensional (2D) plane of OH groups set by the mineral surface is often incommensurate with the tetrahedral H-bond network of water, and how the surface and bulk water networks interact can determine the structure and dynamics of the interface. The interfacial H-bond network then determines many properties of the interface, including surface charging behavior,^{6,7}

dissolution rate,⁸ and catalytic performance.⁹ These mineral–water interfaces are ubiquitous in the outer Earth, and so they also have many important applications in geochemistry,¹⁰ catalysis,^{9,11,12} the carbon cycle,^{13,14} agricultural productivity,^{15,16} and pollution control.^{17,18} Therefore, it is imperative that we fully understand the structure and dynamics of the interfacial H-bond network at the mineral–water interfaces so that we are able to predict behavior across a wide range of mineral compositions, surface terminations, and environmental conditions.

Although the structure of the interfacial H-bond network is important for predicting the properties of oxide–water interfaces, it is often necessary to infer the structure through vibrational spectroscopy. The low charge density of H makes it essentially invisible to X-rays, and the low mass and large incoherent cross section of H lead to multiple complications for neutron scattering,¹⁹ thereby precluding direct measurement of the H-bond network. One can instead infer characteristics of the H-bond network from vibrational probes,

Received: March 23, 2018

Revised: July 13, 2018

Published: September 5, 2018

such as IR and Raman spectroscopy, as the OH stretching frequency depends sensitively on the H-bond strength and thereby the H-bond length.²⁰ However, the greatest challenge with any interface is the thickness: even at a charged interface, the fluctuations in the density profile of water induced by the surface are typically damped within 1–2 nm.²¹ Because any linear spectroscopic probe will sample the bulk water in addition to the interface, the interfacial signal will be completely buried beneath the bulk response. This problem can sometimes be circumvented by using special experimental geometries with high surface–volume ratios, e.g., nanoparticles.²⁰ However, these geometries often expose a number of different surface terminations with different properties, and many oxides have high dissolution rates, which preclude the creation of nanoparticles.²² Instead, the best approach is to use a nonlinear spectroscopic probe such as vibrational sum frequency generation (vSFG).²³ As the vSFG response is proportional to the second-order response function $\chi^{(2)}$, and as $\chi^{(2)}$ is identically zero in a centrosymmetric bulk in the dipole approximation, vSFG provides an interface-specific vibrational probe ideally suited to study mineral–water interfaces.^{24,25}

One of the most important water–mineral interfaces is the aluminum–oxide–water interface, otherwise known as an alumina–water interface. Because alumina has a low dissolution rate, stable surface structure,^{26,27} and can form stable thin films,²⁸ it is important in catalysis^{11,29,30} and microelectronics.^{12,31} In addition, due to its ubiquity in the environment, the ability of the alumina–water interface to adsorb organic and inorganic compounds is important for health and environmental chemistry.³²

The alumina–water interface is interesting from a fundamental perspective due to the high density of the OH groups on all surfaces and how they are arranged on different surface terminations. For instance, the highly ordered and flat (0001) surface features only the $>Al_2OH$ group,^{33–35} whereas the corrugated (11 $\bar{2}0$) surface features $>Al_3OH$, $>Al_2OH$, and $>Al_1OH$ at different heights above the surface plane^{36,37} where $>$ represents a surface-bound group. These different structures often lead to very different experimental results, such as differences in X-ray reflectivity (XRR), vSFG, and IR results. Due to the complexity of the interactions, however, the microscopic origin of many surface spectroscopic features is not clear, and insight from computational models is required for a complete understanding of the interface.

Recent X-ray reflectivity (XRR)^{33,36} and vSFG^{38,39} measurements are interpreted to suggest that the water at the (0001) interface is more ordered and has weaker H-bonds than the water at the (11 $\bar{2}0$) interface. These ideas are supported by the presence a single peak in the density profile of the water at the (0001) interface obtained from fits to the XRR data,³³ as opposed to the multiple peaks in the water density profile at the (11 $\bar{2}0$) interface.³⁶ This is also supported by a blue-shift in the vSFG spectrum of the (0001) vs the (11 $\bar{2}0$) interface, indicating the presence of weaker H-bonds.^{38–41} However, as mentioned earlier, the (0001) surface is flat, whereas the (11 $\bar{2}0$) is corrugated, which could provide an alternative explanation to the differences in the water density profiles. Further, although part of the vSFG spectrum of the (0001) interface is blue-shifted, it actually displays two peaks, one of low frequency around 3250 cm^{-1} and one of high frequency around 3450 cm^{-1} , whereas the vSFG spectrum for the (11 $\bar{2}0$) interface displays a dominant peak around 3250 cm^{-1} . In addition, density functional theory molecular dynamics (DFT-

MD) simulations have shown there can be both weak and strong H-bonds at the alumina (0001) interface.³

Therefore, to characterize the structure and dynamics of the H-bond network at the alumina (0001) and (11 $\bar{2}0$) interface and how they impact the vSFG spectrum, we have run density functional theory molecular dynamics (DFT-MD) simulations of the interfaces. Though other authors have used DFT-MD to study the structure and dynamics of the alumina (0001) interface,^{3,42} little work has been done on the (11 $\bar{2}0$) interface, and a theoretical SFG spectrum has been produced only for the (0001) interface.⁴³ Thus, we characterize the dynamics of the interfacial H-bond network using the H-bond lifetime and the H vibrational density of states (VDOS), characterize the order of the H-bond network using the tetrahedral order parameter,⁴⁴ and calculate the vSFG spectrum from the atomic trajectories. We then compare our calculated vSFG results with measured spectra of the (0001) and (11 $\bar{2}0$) alumina–water interfaces. We find that the water at the alumina (0001) interface is more ordered than that at the (11 $\bar{2}0$) interface, with significantly longer H-bond lifetimes. We also find that, although the water–water H-bonds are relatively of the same strength at both interfaces, the surface–water H-bonds are much weaker at the (0001) vs (11 $\bar{2}0$) interface, which may explain the longer vibrational lifetime at the (0001) vs (11 $\bar{2}0$) interface.³⁸ Finally, we find the apparent blue-shift in the vSFG spectrum for the alumina (0001) vs (11 $\bar{2}0$) interface is primarily due to contributions from the surface OH groups,³ illustrating the importance of the theory of decomposition of the vSFG spectrum, as the mineral surface can play an active role in contributing to the vSFG spectrum.

■ EXPERIMENTAL DETAILS—OPTICAL SETUP

The sample preparation has been described previously^{38,39,40} and is included in the Supporting Information (SI). Approximately 90% of a Ti/sapphire regenerative amplifier laser system (Coherent, LIBRA—F-1K-110-HE+), operating at 1 kHz generating 5 mJ pulses at 800 nm with a pulse duration of 120 fs, pumps a commercial optical parametric amplifier (Coherent, TOPAS-Prime HE). The remaining 500 mW of LIBRA output is passed through a narrow bandpass filter resulting in ~ 30 mW with ~ 2 nm of bandwidth (~ 30 cm^{-1}) for use as the visible beam in vSFG. A removable difference frequency generation AgGaS₂ (AgS) crystal attached to the output of the TOPAS generates tunable pulses in the mid-IR region (4000–1600 cm^{-1}). To collect the vSFG spectra over a region 800 cm^{-1} wide in the OH stretch region, a broadband IR pulse profile is generated with ~ 10 μJ /pulse centered at 3200–3400 cm^{-1} . The incident angles were 60° (IR ~ 5 μJ /pulse) and 54° (visible ~ 30 μJ /pulse) for the steady-state vSFG measurements with focused beam waists of ~ 75 and 200 μm , respectively. The incident angles were chosen to be close to the critical angle to ensure total internal reflection (TIR) to increase the magnitude of our collected vSFG signal and to ensure that we are sampling primarily the χ_{zzz} element of the nonlinear susceptibility $\chi_{eff}^{(2)}$ in PPP polarization.³⁸ Reflected visible SFG photons were separated from scattered 800 nm with a 750 nm shortpass filter (Melles Griot) and sampled via a charge coupled device detector (Princeton Instruments) coupled to a spectrograph (300i Acton Research Corp.). Steady-state vSFG spectra were normalized via division of the nonresonant vSFG signal generated by a gold-coated α -Al₂O₃(0001) prism to account for the IR pulse profile and a second division by appropriate

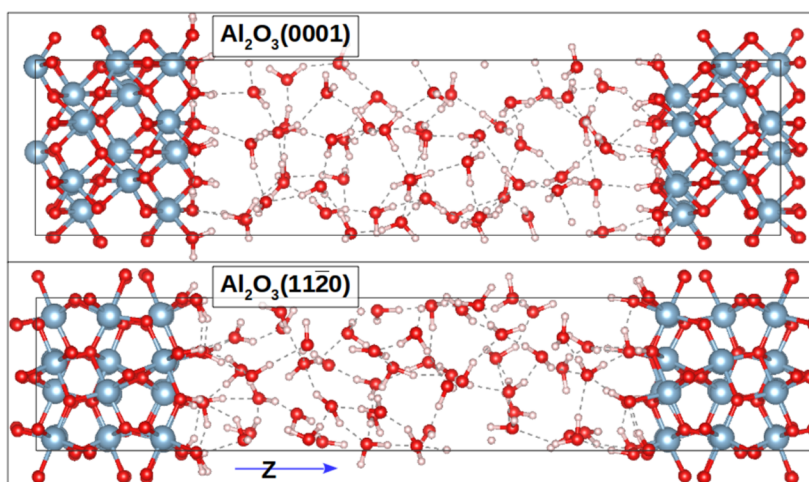


Figure 1. Cells and representative geometry used in the DFT-MD simulations of the $\text{Al}_2\text{O}_3(0001)\text{-H}_2\text{O}$ and $\text{Al}_2\text{O}_3(11\bar{2}0)\text{-H}_2\text{O}$ interfaces. The z -axis is parallel to the surface normals, and the vacuum gap is 2 nm wide.

wavelength-dependent Fresnel factors to correct for the IR dispersion of water.³⁹

■ COMPUTATIONAL DETAILS

We modeled both alumina interfaces using a six-layer Al_2O_3 slab, as XRR experiments have shown that this slab thickness is enough to reproduce the observed surface relaxations.^{33,36} We cleaved the (0001) and (11 $\bar{2}$ 0) surfaces from the ideal crystal geometry using the surface builder module of Materials Studio v7.0⁴⁵ such that both surfaces were terminated by O atoms. We passivated both surfaces with H atoms, as it has been shown that dissociative adsorption of H_2O is favored on both (0001)^{35,46–50} and (11 $\bar{2}$ 0).^{37,47} We then expanded the unit cell of the two alumina surfaces, generating final unit cells with dimensions ($8.243 \times 9.518 \times 20.0 \text{ \AA}$) and ($6.996 \times 10.25961 \times 25.0 \text{ \AA}$) for the (0001) and (11 $\bar{2}$ 0) surfaces, respectively, corresponding to a surface with 12 OH groups for both faces.

To overcome the sampling problems associated with the relatively small cells and short simulation times necessary with DFT-MD, we ran five independent simulations for each surface. We equilibrated the simulations using classical molecular dynamics (CMD) simulations using the ClayFF force field⁵¹ and the LAMMPS simulation package.⁵² The cells were initialized with 10 nm of vacuum populated with H_2O molecules using the PACKMOL code.⁵³ Then, we ran CMD in the NVT ensemble at 423 K for 1 ns, reduced the gap to 2 nm over 1 ns, reduced the temperature to 300 K for 1 ns, and finally equilibrated the system at 300 K for 1 ns. We used this procedure to ensure that H_2O molecules had the time and freedom to find their equilibrium orientation at each alumina interface. We chose a gap of 2 nm, as the CMD simulations have shown that the oscillations in the density profile are damped within ~ 1 nm for a wide range of oxide–water interfaces.^{21,54,55} Thus, the final cell dimensions are ($8.2428 \times 9.518 \times 35.0 \text{ \AA}$) and ($6.99640 \times 10.260 \times 36.6 \text{ \AA}$) for the (0001) and (11 $\bar{2}$ 0) interfaces, respectively. We placed 52 and 48 H_2O molecules in the gap for the (0001) and (11 $\bar{2}$ 0) interfaces, respectively, to achieve water densities of 0.998 g/ cm^3 , as calculated from the volume of the cell occupied by H_2O molecules. The simulation cells used for each interface are shown in Figure 1.

Once the equilibration of the initial structures was completed, all subsequent calculations were performed using

plane-wave-based DFT as implemented in the Vienna ab initio simulation package (v.5.3.5).^{56–59} We used the projector-augmented wave^{60,61} method and the Perdew–Burke–Ernzerhof^{62,63} functional with the Tkatchenko–Scheffler⁶⁴ van der Waals corrections (PBE–TS), as this functional has been shown to result in a reasonably accurate model of water without resorting to expensive exact exchange methods.^{65–67} We also investigated the effect of the choice of the functional by running the (11 $\bar{2}$ 0) interface with the revised PBE (RPBE) functional,⁶⁸ which improves the atomization and surface-binding energies of a wide range of molecules,⁶⁹ in addition to giving a better description of the structure and dynamics of water.⁷⁰ For each interface and functional, we first relaxed the system, equilibrated it using an NVT ensemble, and then ran 27.5 ps production simulations in the NVE ensemble.

We calculated the second-order response function $\chi^{(2)}$, and thereby the vSFG spectrum, using a time-dependent representation^{71,72} where the response function is written as the Fourier transform of the time correlation function between the polarizability and dipole moment derivatives

$$\chi^{(2)} = (i\omega kT)^{-1} \mathcal{F}[\langle \dot{\alpha}(t) \dot{\mu}(0) \rangle] \quad (1)$$

where \mathcal{F} denotes the Fourier transform and $\dot{\alpha}(t)$ and $\dot{\mu}(t)$ are the time derivatives of the polarizability and dipole moment of the system, respectively. We use the time derivative to enforce signals with a zero time average, thereby reducing the noise in the final spectrum. The correlation function is windowed in the time domain using a Blackman–Harris window,⁷³ and a Gaussian filter is applied in the frequency domain to smooth the final spectrum. Note that the correlation function is calculated in the frequency domain as a product of the Fourier transforms of $\dot{\alpha}(t)$ and $\dot{\mu}(t)$, and so the correlation function includes all the correlation lengths in the simulation, from 0.0005 to 27.5 ps. Note also that, because $\dot{\alpha}(t)$ and $\dot{\mu}(t)$ are the sums over the bond polarizabilities and dipole moments, all the correlations between the OH groups are taken into account. We do not truncate the cross-correlation terms, partly due to the small size of our simulation cell and partly because including the cross-correlation contribution to the SFG spectrum is important for damping the surface contributions at the (0001) interface and thereby obtaining an accurate SFG spectrum (see the SI for details) when calculating $\chi^{(2)}$. Once

we obtain $\chi^{(2)}$, we can calculate the vSFG intensity using the following expression

$$I(\Omega) = \frac{8\pi^3\Omega^2 \sec^2(\theta)}{c^3[\epsilon(\Omega)\epsilon(\omega_V)\epsilon(\omega_{IR})]^{1/2}} |\vec{e}_I(\Omega)\chi^{(2)}(\Omega)\vec{e}_J(\omega_V)\vec{e}_K(\omega_{IR})| I(\omega_{IR})I(\omega_V) \quad (2)$$

where \vec{e}_I are polarization vectors, where (I,J,K) can be either S or P, denoting S- and P-polarized light, and $I(\omega)$ is the intensity of the beam with the given frequency. The azimuthal angle θ is taken from the experimental geometry, the spectra are averaged over the polar angle ϕ . $\epsilon(\omega)$ are the frequency-dependent relative permittivities for the bulk materials on either side of the interface, in this case alumina and water, whose values were taken from the experiment.^{74,75} Note that the polarization vectors \vec{e}_I are not Fresnel-factor corrected, as the Fresnel factors are instead removed from the experimental spectrum.

We calculate the polarizabilities and dipole moments of the interfaces using a recently developed bond polarizability model that requires only the atomic trajectories at the interface. Although the details of the method are described elsewhere,⁴³ we briefly review the method here. We first use Thole's method to calculate the additive and effective polarizabilities for each atom in the system.^{76,77} These effective polarizabilities are obtained by inverting the equation: $\mu_i = \mu_i^{(0)} + \alpha_i^{(0)}(E + T_{ij}\mu_j)$. Note we invert this equation exactly, thereby using the full induced dipole model rather than using a first-order approximation.⁷⁸ Here, μ_i and α_i are the dipole and polarizability of the i^{th} atom, respectively, E is an externally applied electric field, and T_{ij} is a short-range corrected dipole interaction matrix. The sum over the resultant effective polarizabilities α_i^{eff} has been shown to accurately reproduce the ab initio molecular polarizability for a wide range of molecules.^{79,80}

Once α_i^{eff} have been obtained, we define the bond polarizability as a linear combination of effective atomic polarizabilities. Coupling these bond polarizabilities with reasonable initial atomic charges, we can calculate self-consistent bond dipoles, which are accurate enough for IR spectroscopy (see SI). Indeed, this bond polarizability model has previously been used to calculate and decompose the vSFG spectrum of the $\text{Al}_2\text{O}_3(0001)\text{-H}_2\text{O}$ interface.⁴³ In this article, we use this model to calculate the vSFG spectrum of $\text{Al}_2\text{O}_3(0001)$ for a different polarization and compare it to the vSFG spectrum of the $(11\bar{2}0)$ interface to inform interpretations of the interfacial structure from the experimental results. Note that the bond position for the O–H bonds is located halfway between the atoms, but we find that the definition of the bond position does not significantly impact the SFG spectrum at the alumina–water interface (see the SI for details).

When calculating the bond polarizabilities and dipole moments, we must take into account the geometry of the unit cell, which has two opposing interfaces. To ensure that we calculate the response of only one interface at a time, we apply a step-function like profile to the cell such that all polarizabilities and dipoles are multiplied by this function before calculating $\chi^{(2)}$. If we position the profile such that it is centered over the interface and includes only the half of the unit cell occupied by that interface, the only bonds with nonzero polarizabilities and dipoles will be those associated with the chosen interface. To prevent erroneous signals due to a sharp cutoff function, we use error functions on the edges

such that the bond properties smoothly go to zero. The profile can then be written as

$$f(x) = \text{sign}(x) \begin{cases} 0.5 \times \text{erfc}(-(x - c_1)/\sqrt{2}\sigma), & x < 0.5(c_1 + c_2) \\ 0.5 \times \text{erfc}((x - c_2)/\sqrt{2}\sigma), & x > 0.5(c_1 + c_2) \end{cases} \quad (3)$$

where $\text{erfc}(x)$ is the complementary error function, c_1 and c_2 are the bottom and top edges of the profile, respectively, σ is the standard deviation of the error function, and the sign function indicates a switch in the orientation of the opposing interfaces such that all SFG calculations have the same coordinate system for the interface. Therefore, our procedure is to assign the nominal atomic charges and polarizabilities, apply the profile to isolate one interface, use 2D Ewald sums and a three-dielectric image model⁸¹ to accurately model the electrostatics of an interface between two semi-infinite dielectrics, and find and use the interaction matrices to calculate the effective polarizabilities and the self-consistent dipole moments.

Finally, when calculating the SFG spectrum, we must also consider the effect of $\chi^{(3)}$. At charged surfaces, the total $\chi^{(2)}$, denoted as $\chi_{\text{eff}}^{(2)}$, is a sum of the nominal second-order response function $\chi^{(2)}$ and the third-order response function $\chi^{(3)}$

$$\chi_{\text{eff}}^{(2)} = \chi^{(2)} + \chi^{(3)} \times E_s \quad (4)$$

where E_s is the electric field at the surface. Although the $\chi^{(3)}$ term can be equal to or larger than $\chi^{(2)}$ at highly charged surfaces with large electric fields, we do not expect the $\chi^{(3)}$ effect to be important for the interfaces we are studying. The $\chi^{(3)}$ effect is generally attributed to induced molecular orientation at the interface, and our simulations show that at a fully protonated $\text{Al}_2\text{O}_3(0001)$ or $(11\bar{2}0)$ surface, there is very little net orientation beyond the first water layer (SI). Thus, we do not expect the $\chi^{(3)}$ effect to be important for these systems.

RESULTS AND DISCUSSION

Using the methods described in the previous sections, we calculate the vSFG spectrum of the $\text{Al}_2\text{O}_3(0001)\text{-H}_2\text{O}$ and $\text{Al}_2\text{O}_3(11\bar{2}0)\text{-H}_2\text{O}$ interfaces. The parameters used to calculate the polarizabilities are fit to H_2O and $\text{Al}(\text{OH})_3$ (SI), and we take the initial charges of the atoms from the ClayFF force field.⁵¹ The vSFG spectrum for the (0001) interface is shown in Figure 2 and the spectrum for the $(11\bar{2}0)$ interface is shown in Figure 3.

We see good agreement between the spectra calculated from the PBE–TS simulations and the experimental spectra, with both showing a peak around 3450 cm^{-1} and a second, less well-defined peak around 3150 cm^{-1} . For the $\text{Al}_2\text{O}_3(0001)\text{-H}_2\text{O}$ interface, we find that the 3150 cm^{-1} peak arises mainly from the surface H_2O molecules, whereas the 3450 cm^{-1} peak has a strong contribution from the surface OH groups. On the other hand, in the $\text{Al}_2\text{O}_3(11\bar{2}0)\text{-H}_2\text{O}$ interface, we find that both H_2O molecules and surface OH groups contribute to the broad peak from 3400 to 3600 cm^{-1} . It is interesting that including the contribution of the in-plane aluminols is important for the correct shape of the spectrum at the (0001) interface, as we expect the $\chi_{zzz}^{(2)}$ term to be dominant for the PPP polarization in TIR geometry.⁸² However, whereas the other components of $\chi^{(2)}$ are smaller than the $\chi_{zzz}^{(2)}$ term, the

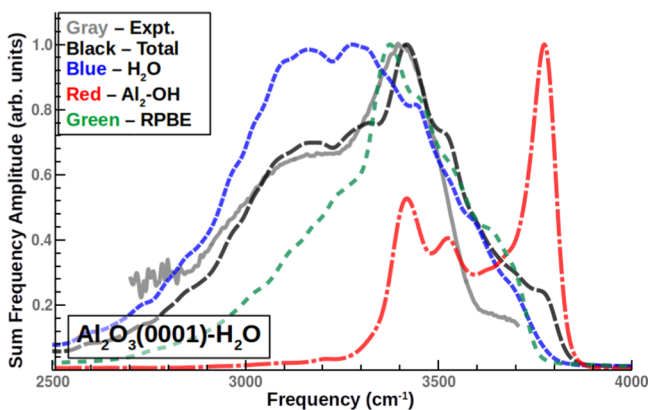


Figure 2. vSFG spectrum for the PPP polarization at the $\text{Al}_2\text{O}_3(0001)\text{-H}_2\text{O}$ interface. The gray line is the experimental spectrum, the black dashed line is the total calculated spectrum, the blue dotted line is the spectrum calculated from only H_2O molecules, the red dashed-dotted line is the spectrum calculated only from surface OH groups, and the green widely dotted line is the total calculated spectrum for the RPBE functional, red-shifted by 100 cm^{-1} . All the experimental and calculated spectra have been normalized to their respective maxima to display them all on the same axes. The total calculated spectrum is not simply related to the H_2O and OH spectra but should roughly resemble the sum of the two.

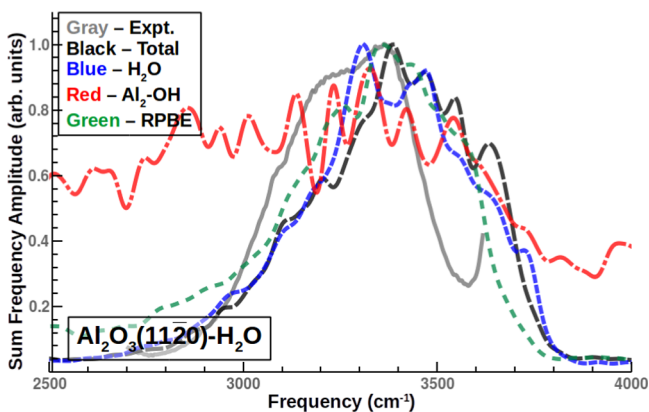


Figure 3. vSFG spectrum for the PPP polarization at the $\text{Al}_2\text{O}_3(11\bar{2}0)\text{-H}_2\text{O}$ interface modeled using the PBE-TS functional. The gray line is the experimental spectrum, the black dashed line is the total calculated spectrum, the blue dotted line is the spectrum calculated from only H_2O molecules, the red dashed-dotted line is the spectrum calculated only from surface OH groups, and the green widely dotted line is the total calculated spectrum for the RPBE functional, red-shifted by 100 cm^{-1} . All the experimental and calculated spectra have been normalized to their respective maxima to display them all on the same axes. The total calculated spectrum is not simply related to the H_2O and OH spectra but should roughly resemble the sum of the two.

other components are still nonzero and the in-plane aluminols are not perfectly parallel to the interface, thereby allowing the in-plane aluminols to have a nonzero contribution to the PPP spectrum. Additionally, we will show below that H_2O donates moderately strong H-bonds to the in-plane aluminols, and so coupling between the interfacial H_2O and the in-plane aluminols may lead to greater intensity of the 3450 cm^{-1} peak. Finally, note that the calculated spectra at the $(11\bar{2}0)$ interface is slightly broader than the experimental spectrum and are blue-shifted. This discrepancy could disappear if a more accurate method was used, such as a meta-generalized

gradient approximation or hybrid functional, or if one ran much longer simulations. Both of these solutions require significant computational resources; however, at our current level of theory, we find the agreement to be acceptable given the associated computational cost.

Interestingly, when we model both the (0001) and $(11\bar{2}0)$ interfaces using the RPBE functional, we actually find worse agreement with experiment than with the PBE-TS functional. This is especially true for the (0001) interface, where the RPBE functional completely fails to capture the low-frequency peak. This is a surprising result, as RPBE does not overbind the H-bonds as much as PBE-TS and gives a better description of the structure and dynamics of water.⁷⁰ Part of the discrepancy between the PBE-TS and RPBE spectra is due to the fortuitous error cancellation of the PBE-TS functional, which gives a reasonable IR spectrum of water despite not including nuclear quantum effects, exact exchange, or long-range dispersion forces.⁸³ To compare the spectra calculated from the PBE-TS and RPBE simulations, we red-shifted the RPBE spectra by 100 cm^{-1} because this shift aligns the maxima of the OH stretching peak of the H VDOS of the H_2O molecules calculated from the two functionals (see SI). Even after red-shifting the RPBE spectrum in Figures 2 and 3, we still find that the RPBE functional generally fails to capture the low-frequency modes at both interfaces, including the main contributions from water at the (0001) interface and the low-frequency shoulder at the $(11\bar{2}0)$ interface. This suggests that the RPBE functional fails to capture strong H-bonds associated with the surface H_2O molecules, which are essential for reproducing the lower-frequency features of the vSFG spectrum.

To better understand the differences in the vSFG spectra, we plot the VDOS of the surface H atoms. Specifically, we plot the VDOS of the H atoms in the first water layer and the surface OH groups, or aluminols, for the $\text{Al}_2\text{O}_3(0001)$ and $\text{Al}_2\text{O}_3(11\bar{2}0)$ interfaces, for both the PBE-TS and RPBE functionals, in Figures 4 and 5, respectively. Additionally, we project the velocities of the aluminols along the surface normal and the surface plane, thereby obtaining the VDOS of the aluminols along those directions. Note that we also projected the VDOS of the surface H_2O molecules along the directions mentioned above, but we found no significant differences in the VDOS. We find that the H_2O and the aluminol modes are somewhat separated at the $\text{Al}_2\text{O}_3(0001)$ interface, especially the out-of-plane modes, and the aluminols tend to occupy distinct vibrational states at the interface. Meanwhile, for both $\text{Al}_2\text{O}_3(11\bar{2}0)$ simulations, the VDOS of the aluminols is much broader and strongly overlaps with the H_2O VDOS. These plots imply that, at the (0001) interface, whereas H_2O donates moderately strong H-bonds to the surface (i.e., $3000\text{--}3500\text{ cm}^{-1}$), the surface aluminols donate only very weak H-bonds with adsorbed H_2O molecules (in agreement with previous work^{3,42}). At the $(11\bar{2}0)$ interface on the other hand, strong H-bonds are donated from H_2O to aluminols and vice versa, and aluminols are able to form strong intrasurface H-bonds with other aluminol groups. Thus, from the VDOS, it would appear that, to obtain an accurate vSFG spectrum, one must accurately model the strong H-bonds at the alumina-water interface, which leads to the separation of water and surface modes at the (0001) interface and are responsible for the long, low-frequency tail at the $(11\bar{2}0)$ interface.

To get a better understanding of the origin of the differences in the vSFG spectra, we analyze the properties of the interfacial

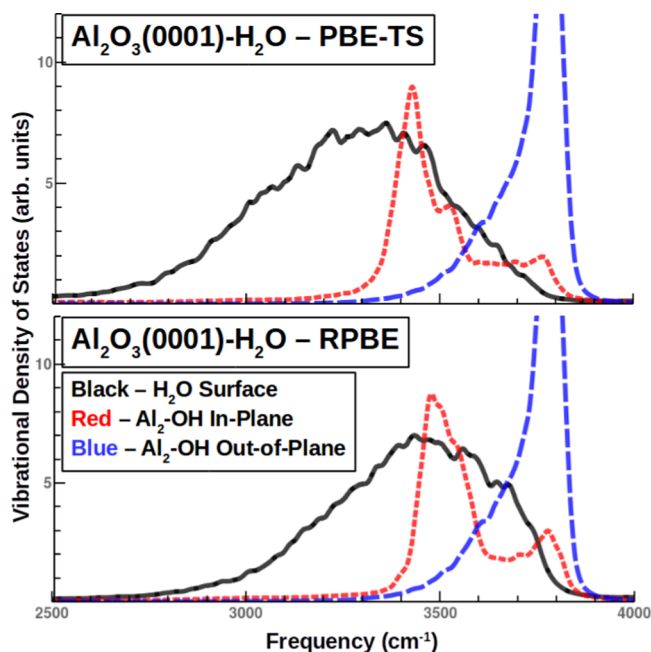


Figure 4. VDOS of the H atoms for the $\text{Al}_2\text{O}_3(0001)\text{-H}_2\text{O}$ interface: the black line is calculated from the first layer of H_2O at the interface, the blue dashed line is calculated from the surface OH groups and projected along the surface normal, and the red dotted line is calculated from the surface OH groups and projected parallel to the surface.

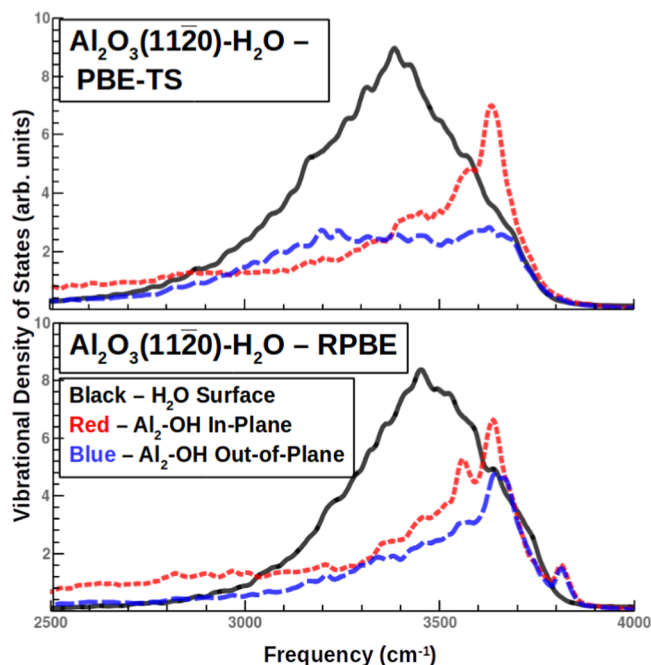


Figure 5. VDOS of the H atoms for the $\text{Al}_2\text{O}_3(11\bar{2}0)\text{-H}_2\text{O}$ interface: the black line is calculated from the first layer of H_2O at the interface, the blue dashed line is calculated from the surface OH groups and projected along the surface normal, and the red dotted line is calculated from the surface OH groups and projected parallel to the surface.

H-bond network. Because the dynamics and the orientation of the H_2O molecules and the surface OH groups are expected to impact the vSFG spectrum, we should expect the number of H-bonds at the surface and their lifetimes to also have a strong

impact on the spectrum. Thus, in Table 1, we list the average number of intrasurface H-bonds ($\langle N_{s-s} \rangle$), the average number of H-bonds from water to the surface ($\langle N_{w-s} \rangle$), the average number of H-bonds donated from the surface aluminols to water ($\langle N_{s-w} \rangle$), the average H-bond lifetime ($\langle t_H \rangle$), and the network decay constant for each of the simulations ($\langle \tau_H \rangle$). Note that we define the H-bond lifetime using a distance and angle cutoff of 2.3 Å and 30°, respectively, with the angle defined as that between the O–H covalent bond and the line connecting two O atoms of the H-bond. Also recall that there are 12 aluminols per surface, and so each simulation can have a total of 24 intrasurface or surface–water H-bonds. The network decay constant is defined as the exponential decay constant associated with the fraction of H-bonds still present at time t , with a given initial network at time t_0 . This network decay constant thus reflects the speed of the global change of the H-bond network, rather than an average over H-bonds, and therefore can lend insight into the stiffness of the network as a whole.⁸⁴

Focusing first on the number of H-bonds at the interface, for both the PBE–TS and RPBE functionals, we find that there are fewer surface–water H-bonds at the (11 $\bar{2}0$) vs (0001) interface, but there are a significantly larger number of intrasurface H-bonds and a larger number of H-bonds in total. This helps explain the difference in the aluminol VDOS: at the (0001) surface, the lattice spacing results in weak intrasurface H-bonds with large H-bond lengths; this manifests as a smaller number of intrasurface H-bonds, but a slightly larger number of surface–water H-bonds compared to the (11 $\bar{2}0$) interface. At the (11 $\bar{2}0$) interface on the other hand, the aluminols are able to form a strong intrasurface H-bonds, leading to a larger number of total H-bonds, a broader VDOS, but slightly fewer surface–water H-bonds.

The H-bond dynamics of the interface illustrate more complex behavior, with each functional displaying different trends when moving from one interface to the other. When using the PBE–TS functional, the H-bond dynamics at the (11 $\bar{2}0$) interface are significantly faster than that at the (0001) interface, with both having shorter average H-bond lifetimes and faster network decay time (Table 1). On the other hand, when using the RPBE functional, we see the opposite result: the dynamics of the (11 $\bar{2}0$) interface are slower than that of the (0001) interface, with smaller $\langle t_H \rangle$ and $\langle \tau_H \rangle$. Note that when going from the (0001) interface to the (11 $\bar{2}0$) interface, for both functionals, the changes in both $\langle t_H \rangle$ and $\langle \tau_H \rangle$ are roughly the same, suggesting that the majority of the H_2O molecules and aluminols in the simulation have shorter/longer H-bond lifetimes rather than a large change in a small minority. Although it is not clear why we see such a discrepancy in the H-bond lifetimes between the two functionals, we believe it might be due to the presence of weaker surface–water H-bonds at the (0001) interface in the RPBE vs PBE–TS simulations. The VDOS in Figure 4 shows that there is a large shift from low to high frequencies in both the H_2O and out-of-plane aluminol modes, with the aluminol mode losing intensity at the low-frequency shoulder and gaining intensity in the peak at $\sim 3750\text{ cm}^{-1}$. Although we cannot directly relate the H-bond strength to the H-bond dynamics at this interface, we hypothesize that these weaker surface–water H-bonds, along with the generally weaker H-bonds of RPBE, lead to the dramatic decrease in the lifetimes when going from PBE–TS to RPBE at the (0001) interface. As for the (11 $\bar{2}0$) interface, the VDOS obtained from RPBE and PBE–TS are quite

Table 1. H-Bond Number and Lifetimes at the Alumina–Water Interfaces

system	(0001)-PBE-TS	(0001)-RPBE	(11 $\bar{2}$ 0)-PBE-TS	(11 $\bar{2}$ 0)-RPBE
$\langle N_{s-s} \rangle$	3.8	3.7	6.45	6.5
$\langle N_{w-s} \rangle$	3.9	2.8	2.3	1.9
$\langle N_{s-w} \rangle$	3.2	2.7	3.2	2.4
$\langle t_H \rangle$ (ps)	0.35	0.16	0.29	0.20
$\langle \tau_H \rangle$ (ps)	7.5	0.6	3.0	1.0

similar, and correspondingly there is not as much of a decrease in lifetimes when going from RPBE to PBE-TS.

Because the H-bond dynamics are closely tied to the H-bond structure, we next investigate the structure of the oxide–water interface by plotting the angular distribution function (ADF) of the surface H₂O molecules. We calculate the ADF by binning the cosine of the angles that each OH group of each H₂O molecule makes with the z-axis, which is parallel with the surface normal. Thus, values close to one indicate OH groups parallel to the surface normal, those near zero indicate OH groups parallel to the surface plane, and those near negative one indicate OH groups antiparallel to the surface normal. We plot the ADFs in Figure 6 and find that the orientations of

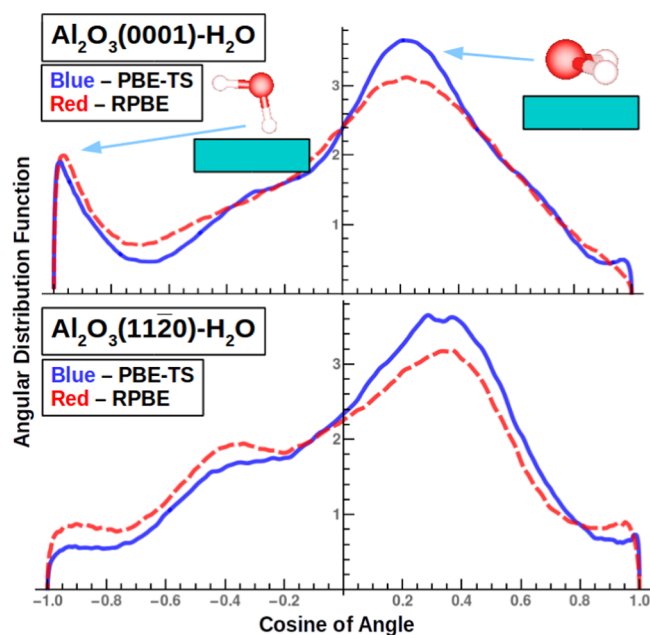


Figure 6. Angular distribution functions (ADFs) of the H₂O molecules in the first water layer at the Al₂O₃ surfaces. The ADF is calculated by binning the cosine of the angle each OH group of each H₂O molecule makes with the surface normal. For each interface, the blue line depicts the ADF for the PBE-TS simulations, whereas the red dashed line depicts the ADF for the RPBE simulations.

H₂O molecules at the (0001) interface differ greatly from those at the (11 $\bar{2}$ 0) interface. The majority of H₂O molecules form H-bonds with other H₂O molecules (roughly 85%), whereas around 15% point out of solution, in this case donating H-bonds to the alumina surface, a distribution reminiscent of the air–water interface. At the (11 $\bar{2}$ 0) interface on the other hand, there is a much broader distribution of H₂O orientations, with many OH groups of H₂O donating H-bonds to the surface at oblique angles ($\sim 120^\circ$) in addition to the OH groups that are antiparallel to the surface normal. Finally, note that the orientations of the surface H₂O molecules do not differ

dramatically with functional, only growing broader when moving from PBE-TS to RPBE with the general shape remaining unchanged. This seems to indicate that the RPBE functional increases local fluctuations of H-bonds but does not alter the average structure.

The results we have presented are consistent with the picture that the SFG spectrum at the alumina–water interface is highly dependent on the degree of corrugation of the alumina surface, and that proper modeling of how this corrugation affects the interfacial H-bond structure and dynamics is essential to obtain accurate spectra. First, when modeling the (0001) and (11 $\bar{2}$ 0) interfaces, we see significant differences in the results when using the PBE-TS and RPBE functionals. Even though the RPBE functional gives a better description of the properties of bulk water,⁷⁰ it ultimately fails to give the proper vibrational spectrum of the interface. We conclude this from the fact that, unlike the RPBE functional, the PBE-TS vSFG spectrum matches the experimental spectrum and the PBE-TS VDOS matches the previous results using the BLYP functional³ and the PBE-TS functional at higher temperature.⁴² The key issue that prevents us from calculating an accurate vSFG spectrum from the RPBE trajectories is the relative difference between the H₂O vibrational spectrum and that of the surface OH groups. The H-bonds between H₂O molecules are weaker in RPBE, which improves bulk water structure; but we see from Figure 4 that the vibrational modes of the aluminols are barely changed when compared with the PBE-TS simulations. At the (0001) interface, this removes the separation in frequencies between the H₂O and OH vibrational frequencies, which eliminates the ~ 3250 cm⁻¹ peak in the vSFG spectrum. At the (11 $\bar{2}$ 0) interface, the difference between the PBE-TS and RPBE simulations is not as noticeable as both simulations show a significant overlap between the H₂O and aluminol vibrational modes. However, we still see that the vSFG spectra calculated with the RPBE functional are missing intensity at low frequencies seen in the experimental spectra.

The effect of the corrugation of the alumina surface on the SFG spectrum is evident from the structure and dynamics of the H-bond network at the (0001) and (11 $\bar{2}$ 0) interface. At the (0001) interface, we have a flat alumina interface, where all surface O atoms are at the same height. Despite the high density of surface OH groups, the flat surface results in weak H-bonds donated by the surface aluminols to H₂O. These weak surface–water H-bonds then lead to a water structure with distinct in-plane and out-of-plane orientations (Figure 6) and a separation between the surface and solution vibrational modes, as shown in Figure 4, leading to the distinct peaks at ~ 3250 and ~ 3450 cm⁻¹ in the SFG spectrum in Figure 2. On the other hand, the (11 $\bar{2}$ 0) surface is corrugated, with the surface O atoms forming rows with different heights above the first layer of Al atoms. This surface structure facilitates the formation of strong aluminol–H₂O and aluminol–aluminol H-bonds, resulting in a significant overlap in the surface and

solution vibrational modes, as seen in Figure 5. This leads to a narrower vSFG spectrum with no clear separation between contributions from aluminols and H₂O molecules (Figure 3).

These results shed light on recent experiments investigating the structure of the alumina–water interface, showing that counterintuitive results can arise from different H-bond dynamics at different interfaces. Recall that the accepted interpretation of the alumina (0001) and (11 $\bar{2}$ 0) interfaces is that the former is less ordered due to the simpler water structure seen in the XRR experiments and the relative blue-shift in the vSFG spectrum. Our results seem to suggest the opposite: the PBE–TS simulations at the (0001) interface have slower H-bond dynamics and a slightly red-shifted vibrational spectrum compared to the (11 $\bar{2}$ 0) interface, which could possibly indicate that the (0001) interface is more ordered than the (11 $\bar{2}$ 0) interface. However, the H-bond lifetimes and vibrational spectra are only indirect measures of the “order” of the interfacial H-bond network. To make our discussion of the order at the interface more precise, we make use of the tetrahedral order parameter q ⁴⁴

$$q = 1 - \frac{3}{8} \sum_{j=1}^3 \sum_{k=j+1}^4 \left(\cos(\phi_{jk}) + \frac{1}{3} \right)^2 \quad (5)$$

where the sum is over all the angles ϕ_{jk} formed by an H₂O molecule's four nearest neighbors. In ice, $q = 1$, in PBE–TS water, q is around 0.8, and in ideal gas, $q = 0$. Thus, if we calculate q for each H₂O molecule in our simulations, we can get a local measure of the order of the H-bond network and find if it is more ordered ($q = 1$) or disordered ($q = 0$). Note that we include the surface aluminols in our calculation of q , as they serve as H-bonding sites and prevent an artificial reduction in the order parameter near the interface. We plot q for each H₂O molecule vs its average position along the z-axis for the (0001) and (11 $\bar{2}$ 0) interfaces and the PBE–TS and RPBE functionals in Figure 7. What we find matches our intuition from the H-bond dynamics and vibrational spectra: for the PBE–TS functional, the (0001) interface is more ordered than the (11 $\bar{2}$ 0) interface, with the order parameter at the (0001) interface rarely dropping below 0.6, even near the alumina surface. For the RPBE functional on the other hand, we find that the water at the (11 $\bar{2}$ 0) interface is generally slightly more ordered than that at the (0001) interface, except right at the (11 $\bar{2}$ 0) interface, where the order parameter drops below 0.6.

Thus, we find that our conclusions on the order of water at the alumina–water interface for the (0001) and (11 $\bar{2}$ 0) interfaces are opposite to the experimental interpretation, and the results depend strongly upon the choice of the functional. The reason for this difference lies in the difficulty of drawing conclusions on the local structure and dynamics of water using either spectroscopy or methods that measure the average structure, such as XRR. Because XRR only gives the average positions of the water O at the alumina interface, it cannot be tied directly to the local order of the interfacial H-bond network. At the (0001) interface, the single peak in the O density profile is indicative of an ordered interface with longer H-bond lifetimes. At the (11 $\bar{2}$ 0) interface, the interfacial water is actually much less ordered than water at the (0001) interface, and the multiple peaks in the XRR O density profile are primarily due to the surface corrugation. Because vSFG probes only the interfacial region, it is easier to draw conclusions on the interfacial structure. Indeed, recent results

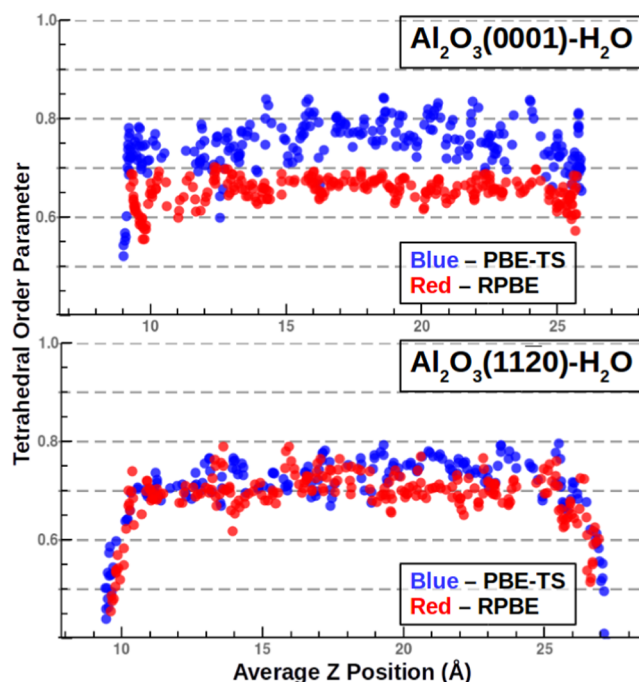


Figure 7. Order parameter q defined in eq 5 for each H₂O molecule plotted with respect to the average position of the O atom in the H₂O molecule. The edges of the x-axis are set to the average position of the terminal O atoms on the alumina surface. The data have been smoothed slightly using a Gaussian filter with width of 1.5 Å to better illustrate the average and trends between the different interfaces and functionals.

have suggested that the blue-shift of the (0001) vs (11 $\bar{2}$ 0) interface is due to a weaker H-bond environment caused by different surface terminations, in agreement with our results showing weaker surface–water H-bonds at the (0001) interface.³⁸ These weaker H-bonds can exist in a more ordered H-bond network at the (0001) interface because a flat surface results in weaker surface–water H-bonds, longer H-bond lifetimes, and larger order parameter.

Finally, our results on the alumina interfaces agree with recent IR–pump–vSFG probe experiments. These experiments have shown that the vibrational dynamics of the O–H stretch of the near-neutral Al₂O₃(0001)–H₂O interface is nearly twice as slow as that of the Al₂O₃(11 $\bar{2}$ 0)–H₂O interface.³⁸ The faster dynamics at the (11 $\bar{2}$ 0) interface was explained in terms of either (1) Förster type energy transfer between different OH groups, (2) the presence of strong (~ 3000 cm⁻¹) H-bonds, and (3) relaxation through photoinduced proton transfer from aluminols to H₂O.³⁹ Our PBE–TS simulations show that there is much stronger overlap in the VDOS of the H₂O and the aluminols at the (11 $\bar{2}$ 0) vs (0001) interface, which would aid in Förster type energy transfer, and we find much stronger intrasurface H-bonds and surface–water H-bonds at the (11 $\bar{2}$ 0) vs (0001) interface. The stronger H-bonds donated by aluminol to H₂O at the (11 $\bar{2}$ 0) interface could also lead to an enhancement of the photoinduced proton transfer, despite the system being less ordered. Clearly, more work must be done to elucidate the mechanism of vibrational relaxation at the alumina–water interface and how it is tied to the surface structure and the interfacial H-bond network.

CONCLUSIONS

In conclusion, we were able to elucidate the structure and dynamics of the interfacial H-bond network at the $\text{Al}_2\text{O}_3(0001)\text{-H}_2\text{O}$ and $\text{Al}_2\text{O}_3(11\bar{2}0)\text{-H}_2\text{O}$ interfaces using DFT-MD simulations. We calculated the vSFG spectrum and showed that the PBE-TS simulations accurately reproduced the experimental spectrum at both (0001) and (11 $\bar{2}0$) interfaces, whereas the RPBE functional failed to accurately reproduce the vSFG spectrum. By studying the VDOS, the H-bond dynamics, and the orientation of the first surface layer of water at the interface, we were able to show that the differences in the spectra of the two interfaces are primarily due to the differences in the H-bond lifetimes and the order of the interfacial H-bond network induced by the different surface terminations. At the (0001) interface in the PBE-TS simulations, the flat plane of aluminols causes a frustration of the water at the interface, leading to weak H-bonds from aluminols to H_2O , long H-bond lifetimes, and ordered H-bond network at the interface. The relatively weak surface-solution interactions thereby lead to the separation of the surface and solution vibrational modes, in turn, leading to well-separated peaks at ~ 3150 and ~ 3450 cm^{-1} . On the other hand, the RPBE functional does not lead to any separation between the surface and the solution modes and is missing amplitude at low frequencies due to a blue-shift of the H_2O H-bond frequencies and a weakening of the aluminol- H_2O H-bonds. Without this separation in the surface and solution modes, the ~ 3250 peak in the SFG spectrum disappears entirely. At the (11 $\bar{2}0$) interface, the corrugated surface leads to stronger surface-solution H-bonds than at the (0001) interface, causing the surface and the solution vibrational modes to occupy the same frequency range. The vSFG spectrum of the (11 $\bar{2}0$) interface therefore has a single band in the range $3200\text{--}3350$ cm^{-1} , with closely spaced peaks. Thus, the apparent blue-shift in the spectrum of the (0001) vs (11 $\bar{2}0$) interface is in fact due to the decoupling of the surface and the solution vibrational modes as a result of the surface structure, not because it is a more disordered interface with weaker H-bonds. Indeed, we find that the (0001) interface is actually more ordered than the (11 $\bar{2}0$) interface, with significantly longer H-bond lifetimes and greater order parameter. Although our peak assignments agree with the vSFG results, our conclusions on the interfacial order are in contrast to the interpretations from the XRR measurements, as they do not take into account surface corrugation when determining the structure of water from the shape of the O density profile.

Clearly, both density and distribution of OH groups on an oxide surface strongly affect the surface-water interactions and thereby the structure and dynamics of the surface H_2O molecules. Future extensions of this work could involve investigating a wide range of different minerals and surface terminations using DFT-MD to determine how surface OH group density, orientation, and distance from the surface plane affect the structure and the dynamics of the interfacial H-bond network. Alternatively, one could study a series of model systems with different surface lattices and height distributions of surface OH groups to more systematically study how these factors affect the H-bond network. Either way, much work must still be done to understand the effect of surface structure and the distribution of OH groups on the structure and dynamics of interfacial water.

ASSOCIATED CONTENT

Supporting Information

The Supporting Information is available free of charge on the ACS Publications website at DOI: 10.1021/acs.jpcc.8b02809.

Radial distribution functions; surface structure; water orientation; density profiles; O-O RDF for O atoms (Figure S1); $\text{Al}_2\text{O}_3(0001)\text{-H}_2\text{O}$ interfacial structure (Table S1, S2); angular distribution of aluminols (Figure S2); water orientation at center of unit cell (Figure S3); axial density profiles (Figure S4-S8); H_2O VDOS (Figure S9-S10); vSFG spectrum-no filter (Figure S11-S12); vSFG spectrum-SSP polarization (Figure S13); vSFG spectrum-effect of correlation cutoff (Figure S15-S16); vSFG-dependence on bond position definition (Figure S17); vSFG calculation details; polarizability parameters for vSFG calculations; real and imaginary parts of $\chi(2)$; alumina sample preparation. (PDF)

AUTHOR INFORMATION

Corresponding Author

*E-mail: eborquet@temple.edu.

ORCID

Mark DelloStritto: 0000-0002-0678-5860

Notes

The authors declare no competing financial interest.

ACKNOWLEDGMENTS

This research includes calculations carried out on Temple University's HPC resources and thus was supported in part by the National Science Foundation through major research instrumentation grant number 1625061 and by the U.S. Army Research Laboratory under contract number W911NF-16-2-0189. This work was supported as part of the Center for the Computational Design of Functional Layered Materials, an Energy Frontier Research Center funded by the US Department of Energy, Office of Science, Basic Energy Sciences under Grant No. DE-SC0012575. The authors acknowledge the National Science Foundation for supporting the experimental aspects of this work (NSF Grant No. CHE 1337880).

REFERENCES

- (1) Kusalik, P. G.; Svishchev, I. M. The Spatial Structure in Liquid Water. *Science* **1994**, *265*, 1219-1221.
- (2) Head-Gordon, T.; Hura, G. Water Structure from Scattering Experiments and Simulation. *Chem. Rev.* **2002**, *102*, 2651-2670.
- (3) Gaigeot, M.-P.; Sprik, M.; Sulpizi, M. Oxide-water interfaces: how the surface chemistry modifies interfacial water properties. *J. Phys.: Condens. Matter* **2012**, *24*, No. 124106.
- (4) Kumar, N.; Neogi, S.; Kent, P. R. C.; Bandura, A. V.; Kubicki, J. D.; Wesolowski, D. J.; Cole, D.; Sofo, J. O. Hydrogen Bonds and Vibrations of Water on (110)Rutile. *J. Phys. Chem. C* **2009**, *113*, 13732-13740.
- (5) Kumar, N.; Kent, P. R. C.; Bandura, A. V.; Kubicki, J. D.; Wesolowski, D. J.; Cole, D. R.; Sofo, J. O. Faster proton transfer dynamics of water on SnO_2 compared to TiO_2 . *J. Chem. Phys.* **2011**, *134*, No. 044706.
- (6) Dove, P. M.; Craven, C. M. Surface charge density on silica in alkali and alkaline earth chloride electrolyte solutions. *Geochim. Cosmochim. Acta* **2005**, *69*, 4963-4970.
- (7) Dewan, S.; Yeganeh, M. S.; Borquet, E. Experimental Correlation Between Interfacial Water Structure and Mineral Reactivity. *J. Phys. Chem. Lett.* **2013**, *4*, 1977-1982.

- (8) Dove, P. M. The dissolution kinetics of quartz in aqueous mixed cation solutions. *Geochim. Cosmochim. Acta* **1999**, *63*, 3715–3727.
- (9) Fujishima, A.; Zhang, X.; Tryk, D. A. TiO₂ photocatalysis and related surface phenomena. *Surf. Sci. Rep.* **2008**, *63*, 515–582.
- (10) Stumm, W. *Chemistry of the Solid-Water Interface: Processes at the Mineral-Water and Particle-Water Interface in Natural Systems*; John Wiley and Sons, Inc.: NY, 1992.
- (11) Freund, H. J.; Bäumer, M.; Libuda, J.; Risse, T.; Rupprechter, G.; Shaikhutdinov, S. Preparation and characterization of model catalysts: from ultrahigh vacuum to in situ conditions at the atomic dimension. *J. Catal.* **2003**, *216*, 223–235.
- (12) Kelber, J. A.; Niu, C.; Shepherd, K.; Jennison, D. R.; Bogicevic, A. Copper wetting of α -Al₂O₃(0001): theory and experiment. *Surf. Sci.* **2000**, *446*, 76–88.
- (13) Berner, R. A. Weathering, plants, and the long-term carbon cycle. *Geochim. Cosmochim. Acta* **1992**, *56*, 3225–3231.
- (14) Berner, R. A.; Lasaga, A. C.; Garrels, R. M. The carbonate-silicate geochemical cycle and its effect on atmospheric carbon dioxide over the past 100 million years. *Am. J. Sci.* **1983**, *283*, 641–683.
- (15) Van Soest, P. Rice straw, the role of silica and treatments to improve quality. *Anim. Feed Sci. Technol.* **2006**, *130*, 137–171.
- (16) Sacala, E. Role of silicon in plant resistance to water stress. *J. Elementol.* **2009**, *14*, 619–630.
- (17) Hua, M.; Zhang, S.; Pan, B.; Zhang, W.; Lv, L.; Zhang, Q. Heavy metal removal from water/wastewater by nanosized metal oxides: A review. *J. Hazard. Mater.* **2012**, *211–212*, 317–331.
- (18) Frugier, P.; Gin, S.; Minet, Y.; Chave, T.; Bonin, B.; Godon, N.; Lartigue, J.-E.; Jollivet, P.; Ayrat, A.; de Windt, L.; et al. SON68 nuclear glass dissolution kinetics: Current state of knowledge and basis of the new GRAAL model. *J. Nucl. Mater.* **2008**, *380*, 8–21.
- (19) Amann-Winkel, K.; Bellissent-Funel, M.-C.; Bove, L. E.; Loerting, T.; Nilsson, A.; Paciaroni, A.; Schlesinger, D.; Skinner, L. X-ray and Neutron Scattering of Water. *Chem. Rev.* **2016**, *116*, 7570–7589.
- (20) Wang, H.-W.; DelloStritto, M. J.; Kumar, N.; Kolesnikov, A. I.; Kent, P. R. C.; Kubicki, J. D.; Wesolowski, D. J.; Sofo, J. O. Vibrational Density of States of Strongly H-Bonded Interfacial Water: Insights from Inelastic Neutron Scattering and Theory. *J. Phys. Chem. C* **2014**, *118*, 10805–10813.
- (21) Dewan, S.; Carnevale, V.; Bankura, A.; Eftekhari-Bafrooei, A.; Fiorin, G.; Klein, M. L.; Borguet, E. Structure of Water at Charged Interfaces: A Molecular Dynamics Study. *Langmuir* **2014**, *30*, 8056–8065.
- (22) Brantley, S. L. *Kinetics of Water-Rock Interaction*; Springer: NY, 2008; pp 151–210.
- (23) Zhu, X. D.; Suhr, H.; Shen, Y. R. Surface vibrational spectroscopy by infrared-visible sum frequency generation. *Phys. Rev. B* **1987**, *35*, 3047–3050.
- (24) Shen, Y. R. *The Principles of Nonlinear Optics*; Wiley, 2003.
- (25) Boyd, R. *Nonlinear Optics*; Elsevier, 2008.
- (26) Gan, Y.; Franks, G. V. High Resolution AFM Images of the Single-Crystal α -Al₂O₃(0001) Surface in Water. *J. Phys. Chem. B* **2005**, *109*, 12474–12479.
- (27) Kurnosikov, O.; Pham Van, L.; Cousty, J. About anisotropy of atomic-scale height step on (0001) sapphire surface. *Surf. Sci.* **2000**, *459*, 256–264.
- (28) Qin, F.; Magtoto, N. P.; Kelber, J. A.; Jennison, D. R. Theory and experiments on the structure of 7 Å alumina films grown on Ni₃Al. *J. Mol. Catal. A: Chem.* **2005**, *228*, 83–87.
- (29) Yadav, O. P.; Palmqvist, A.; Cruise, N.; Holmberg, K. Synthesis of platinum nanoparticles in microemulsions and their catalytic activity for the oxidation of carbon monoxide. *Colloids Surf., A* **2003**, *221*, 131–134.
- (30) Dellwig, T.; Hartmann, J.; Libuda, J.; Meusel, I.; Rupprechter, G.; Unterhalt, H.; Freund, H. J. Complex model catalysts under UHV and high pressure conditions: CO adsorption and oxidation on alumina-supported Pd particles. *J. Mol. Catal. A: Chem.* **2000**, *162*, 51–66.
- (31) Oepts, W.; Verhagen, H. J.; de Jonge, W. J. M.; Coehoorn, R. Dielectric breakdown of ferromagnetic tunnel junctions. *Appl. Phys. Lett.* **1998**, *73*, 2363–2365.
- (32) Kasprzyk-Hordern, B. Chemistry of alumina, reactions in aqueous solution and its application in water treatment. *Adv. Colloid Interface Sci.* **2004**, *110*, 19–48.
- (33) Catalano, J. G. Weak interfacial water ordering on isostructural hematite and corundum (001) surfaces. *Geochim. Cosmochim. Acta* **2011**, *75*, 2062–2071.
- (34) Eng, P. J.; Trainor, T. P.; Brown, G. E., Jr.; Waychunas, G. A.; Newville, M.; Sutton, S. R.; Rivers, M. L. Structure of the Hydrated α -Al₂O₃ (0001) Surface. *Science* **2000**, *288*, 1029–1033.
- (35) Liu, P.; Kendelewicz, T.; Brown, G. E., Jr.; Nelson, E. J.; Chambers, S. A. Reaction of water vapor with α -Al₂O₃(0001) and α -Fe₂O₃(0001) surfaces: synchrotron X-ray photoemission studies and thermodynamic calculations. *Surf. Sci.* **1998**, *417*, 53–65.
- (36) Catalano, J. G. Relaxations and Interfacial Water Ordering at the Corundum (110) Surface. *J. Phys. Chem. C* **2010**, *114*, 6624–6630.
- (37) Sung, J.; Shen, Y. R.; Waychunas, G. A. The interfacial structure of water/protonated α -Al₂O₃ as a function of pH. *J. Phys.: Condens. Matter* **2012**, *24*, No. 124101.
- (38) Tuladhar, A.; Piontek, S. M.; Borguet, E. Insights on Interfacial Structure, Dynamics, and Proton Transfer from Ultrafast Vibrational Sum Frequency Generation Spectroscopy of the Alumina(0001)/Water Interface. *J. Phys. Chem. C* **2017**, *121*, 5168–5177.
- (39) Tuladhar, A.; Dewan, S.; Kubicki, J. D.; Borguet, E. Spectroscopy and Ultrafast Vibrational Dynamics of Strongly Hydrogen Bonded OH Species at the α -Al₂O₃(1120)/H₂O Interface. *J. Phys. Chem. C* **2016**, *120*, 16153–16161.
- (40) Tuladhar, A.; Piontek, S. M.; Frazer, L.; Borguet, E. The Effect of Halide Ions on the Structure and Dynamics of Water Next to an Alumina (0001) Surface. *J. Phys. Chem. C* **2018**, *122* (24), 12819–12830.
- (41) Braunschweig, B.; Eissner, S.; Daum, W. Molecular Structure of a Mineral/Water Interface: Effects of Surface NanoRoughness of α -Al₂O₃(0001). *J. Phys. Chem. C* **2008**, *112*, 1751–1754.
- (42) Huang, P.; Pham, T. A.; Galli, G.; Schwegler, E. Alumina-(0001)/Water Interface: Structural Properties and Infrared Spectra from First-Principles Molecular Dynamics Simulations. *J. Phys. Chem. C* **2014**, *118*, 8944–8951.
- (43) DelloStritto, M.; Sofo, J. Bond Polarizability Model for Sum Frequency Generation at the Al₂O₃(0001)-H₂O Interface. *J. Phys. Chem. A* **2017**, *121*, 3045–3055.
- (44) Errington, J. R.; Debenedetti, P. G. Relationship between structural order and the anomalies of liquid water. *Nature* **2001**, *409*, 318–321.
- (45) Biovia, D. S. *Discovery Studio Modeling Environment*, Materials Studio v.7.0; Dassault Systèmes: San Diego, 2017.
- (46) Elam, J. W.; Nelson, C. E.; Cameron, M. A.; Tolbert, M. A.; George, S. M. Adsorption of H₂O on a Single-Crystal α -Al₂O₃(0001) Surface. *J. Phys. Chem. B* **1998**, *102*, 7008–7015.
- (47) Leeuw, N. H.; Parker, S. C. Effect of Chemisorption and Physisorption of Water on the Surface Structure and Stability of α -Alumina. *J. Am. Ceram. Soc.* **1999**, *82*, 3209–2316.
- (48) Kirsch, H.; Wirth, J.; Tong, Y.; Wolf, M.; Saalfrank, P.; Campen, R. K. Experimental Characterization of Unimolecular Water Dissociative Adsorption on α -Alumina. *J. Phys. Chem. C* **2014**, *118*, 13623–13630.
- (49) Łodziana, Z.; Nørskov, J. K.; Stoltze, P. The stability of the hydroxylated (0001) surface of α -Al₂O₃. *J. Chem. Phys.* **2003**, *118*, 11179–11188.
- (50) Hass, K. C.; Schneider, W. F.; Curioni, A.; Andreoni, W. First-Principles Molecular Dynamics Simulations of H₂O on α -Al₂O₃(0001). *J. Phys. Chem. B* **2000**, *104*, 5527–5540.
- (51) Cygan, R. T.; Liang, J.-J.; Kalinichev, A. G. Molecular Models of Hydroxide, Oxyhydroxide, and Clay Phases and the Development of a General Force Field. *J. Phys. Chem. B* **2004**, *108*, 1255–1266.

- (52) Plimpton, S. Fast Parallel Algorithms for Short-Range Molecular Dynamics. *J. Comput. Phys.* **1995**, *117*, 1–19.
- (53) Martínez, L.; Andrade, R.; Birgin, E. G.; Martínez, J. M. PACKMOL: A package for building initial configurations for molecular dynamics simulations. *J. Comput. Chem.* **2009**, *30*, 2157–2164.
- (54) Argyris, D.; Ho, T.; Cole, D. R.; Striolo, A. Molecular Dynamics Studies of Interfacial Water at the Alumina Surface. *J. Phys. Chem. C* **2011**, *115*, 2038–2046.
- (55) Skelton, A. A.; Fenter, P.; Kubicki, J. D.; Wesolowski, D. J.; Cummings, P. T. Simulations of the Quartz(10 $\bar{1}$ 1)/Water Interface: A Comparison of Classical Force Fields, Ab Initio Molecular Dynamics, and X-ray Reflectivity Experiments. *J. Phys. Chem. C* **2011**, *115*, 2076–2088.
- (56) Kresse, G.; Furthmüller, J. Efficiency of ab-initio total energy calculations for metals and semiconductors using a plane-wave basis set. *Comput. Mater. Sci.* **1996**, *6*, 15–50.
- (57) Kresse, G.; Hafner, J. Ab initio molecular-dynamics simulation of the liquid-metal-amorphous-semiconductor transition in germanium. *Phys. Rev. B* **1994**, *49*, 14251–14269.
- (58) Kresse, G.; Hafner, J. Ab initio molecular dynamics for liquid metals. *Phys. Rev. B* **1993**, *47*, 558–561.
- (59) Kresse, G.; Furthmüller, J. Efficient iterative schemes for ab initio total-energy calculations using a plane-wave basis set. *Phys. Rev. B* **1996**, *54*, 11169–11186.
- (60) Blöchl, P. E. Projector augmented-wave method. *Phys. Rev. B* **1994**, *50*, 17953–17979.
- (61) Kresse, G.; Joubert, D. From ultrasoft pseudopotentials to the projector augmented-wave method. *Phys. Rev. B* **1999**, *59*, 1758–1775.
- (62) Perdew, J. P.; Burke, K.; Ernzerhof, M. Generalized Gradient Approximation Made Simple. *Phys. Rev. Lett.* **1996**, *77*, 3865–3868.
- (63) Perdew, J. P.; Burke, K.; Ernzerhof, M. Erratum: Generalized Gradient Approximation Made Simple. *Phys. Rev. Lett.* **1997**, *78*, 1396.
- (64) Tkatchenko, A.; Scheffler, M. Accurate Molecular Van Der Waals Interactions from Ground-State Electron Density and Free-Atom Reference Data. *Phys. Rev. Lett.* **2009**, *102*, No. 073005.
- (65) Grossman, J. C.; Schwegler, E.; Draeger, E. W.; Gygi, F.; Galli, G. Towards an assessment of the accuracy of density functional theory for first principles simulations of water. *J. Chem. Phys.* **2004**, *120*, 300–311.
- (66) Schwegler, E.; Grossman, J. C.; Gygi, F.; Galli, G. Towards an assessment of the accuracy of density functional theory for first principles simulations of water. II. *J. Chem. Phys.* **2004**, *121*, 5400–5409.
- (67) Gillan, M. J.; Alfè, D.; Michaelides, A. Perspective: How good is DFT for water? *J. Chem. Phys.* **2016**, *144*, No. 130901.
- (68) Hammer, B.; Hansen, L. B.; Nørskov, J. K. Improved adsorption energetics within density-functional theory using revised Perdew-Burke-Ernzerhof functionals. *Phys. Rev. B* **1999**, *59*, 7413–7421.
- (69) Wendt, S.; Schaub, R.; Matthiesen, J.; Vestergaard, E. K.; Wahlström, E.; Rasmussen, M. D.; Thosttrup, P.; Molina, L. M.; Lægsgaard, E.; Stensgaard, I.; et al. Oxygen vacancies on TiO₂(110) and their interaction with H₂O and O₂: A combined high-resolution STM and DFT study. *Surf. Sci.* **2005**, *598*, 226–245.
- (70) Forster-Tonigold, K.; Groß, A. Dispersion corrected RPBE studies of liquid water. *J. Chem. Phys.* **2014**, *141*, No. 064501.
- (71) Morita, A.; Ishiyama, T. Recent progress in theoretical analysis of vibrational sum frequency generation spectroscopy. *Phys. Chem. Chem. Phys.* **2008**, *10*, 5801–5816.
- (72) Khatib, R.; Sulpizi, M. Sum Frequency Generation Spectra from Velocity-Velocity Correlation Functions. *J. Phys. Chem. Lett.* **2017**, *8*, 1310–1314.
- (73) Harris, F. J. On the use of windows for harmonic analysis with the discrete Fourier transform. *Proc. IEEE* **1978**, *66*, 51–83.
- (74) Malitson, I. H. Refraction and Dispersion of Synthetic Sapphire. *J. Opt. Soc. Am.* **1962**, *52*, No. 1377.
- (75) Bertie, J. E.; Ahmed, M. K.; Eysel, H. H. Infrared intensities of liquids. 5. Optical and dielectric constants, integrated intensities, and dipole moment derivatives of water and water-d₂ at 22.degree.C. *J. Phys. Chem.* **1989**, *93*, 2210–2218.
- (76) Applequist, J.; Carl, J. R.; Fung, K.-K. Atom dipole interaction model for molecular polarizability. Application to polyatomic molecules and determination of atom polarizabilities. *J. Am. Chem. Soc.* **1972**, *94*, 2952–2960.
- (77) Thole, B. Molecular polarizabilities calculated with a modified dipole interaction. *Chem. Phys.* **1981**, *59*, 341–350.
- (78) Nagata, Y.; Mukamel, S. Vibrational Sum-Frequency Generation Spectroscopy at the Water/Lipid Interface: Molecular Dynamics Simulation Study. *J. Am. Chem. Soc.* **2010**, *132*, 6434–6442.
- (79) van Duijnen, P. T.; Swart, M. Molecular and Atomic Polarizabilities: Thole's Model Revisited. *J. Phys. Chem. A* **1998**, *102*, 2399–2407.
- (80) Wang, J.; Cieplak, P.; Li, J.; Hou, T.; Luo, R.; Duan, Y. Development of Polarizable Models for Molecular Mechanical Calculations I: Parameterization of Atomic Polarizability. *J. Phys. Chem. B* **2011**, *115*, 3091–3099.
- (81) Barrera, R. G.; Guzmán, O.; Balaguer, B. Point charge in a three-dielectric medium with planar interface. *Am. J. Phys.* **1978**, *46*, 1172–1179.
- (82) Isaienko, O.; Nihonyanagi, S.; Sil, D.; Borguet, E. Observation of the Bending Mode of Interfacial Water at Silica Surfaces by Near-Infrared Vibrational Sum-Frequency Generation Spectroscopy of the [Stretch + Bend] Combination Bands. *J. Phys. Chem. Lett.* **2013**, *4*, 531–535.
- (83) Heyden, M.; Sun, J.; Funkner, S.; Mathias, G.; Forbert, H.; Havenith, M.; Marx, D. Dissecting the THz spectrum of liquid water from first principles via correlations in time and space. *Proc. Natl. Acad. Sci. U.S.A.* **2010**, *107*, 12068–12073.
- (84) DelloStritto, M. J.; Kubicki, J. D.; Sofo, J. O. Effect of Ions on H-Bond Structure and Dynamics at the Quartz(101)-Water Interface. *Langmuir* **2016**, *32*, 11353–11365.